Acta Materialia 163 (2019) 40–54

Contents lists available at ScienceDirect

Acta Materialia

journal homepage: www.elsevier.com/locate/actamat

Full length article

Hierarchical microstructure design to tune the mechanical behavior of an interstitial TRIP-TWIP high-entropy alloy

Jing Su*, Dierk Raabe, Zhiming Li**

Max-Planck-Institut für Eisenforschung, Max-Planck-Str. 1, 40237, Düsseldorf, Germany

ARTICLE INFO

Article history:
Received 8 May 2018
Received in revised form
8 September 2018
Accepted 10 October 2018
Available online 11 October 2018

Keywords:
Interstitials
High-entropy alloys
Recrystallization
Twinning
Martensitic phase transformation

ABSTRACT

We demonstrate a novel approach of utilizing a hierarchical microstructure design to improve the mechanical properties of an interstitial carbon doped high-entropy alloy (HEA) by cold rolling and subsequent tempering and annealing. Bimodal microstructures were produced in the tempered specimens consisting of nano-grains (~50 nm) in the vicinity of shear bands and recovered parent grains (10–35 μm) with pre-existing nano-twins. Upon annealing, partial recrystallization led to trimodal microstructures characterized by small recrystallized grains (<1 μm) associated with shear bands, medium-sized grains (1–6 μm) recrystallized through subgrain rotation or coalescence of parent grains and retained large unrecrystallized grains. To reveal the influence of these hierarchical microstructures on the strength-ductility synergy, the underlying deformation mechanisms and the resultant strain hardening were investigated. A superior yield strength of 1.3 GPa was achieved in the bimodal microstructure, more than two times higher than that of the fully recrystallized microstructure, owing to the presence of nano-sized grains and nano-twins. The ductility was dramatically improved from 14% to 60% in the trimodal structure compared to the bimodal structure due to the appearance of a multi-stage work hardening behavior. This important strain hardening sequence was attributed to the sequential activation of transformation-induced plasticity (TRIP) and twinning-induced plasticity (TWIP) effects as a result of the wide variation in phase stability promoted by the grain size hierarchy. These findings open a broader window for achieving a wide spectrum of mechanical properties for HEAs, making better use of not only compositional variations but also microstructure and phase stability tuning.

1. Introduction

Currently, there is considerable interest in the field of high-entropy alloys (HEAs) not only due to their configurational entropy-driven phase stability of massive solid solutions [1] and in part good mechanical properties [2] but also because they open up a practically infinite compositional space for future solid solution alloy development [3,4]. The original design concept of HEAs was directed towards mixing of more than five alloying elements at near equimolar concentrations with the aim of forming a single-phase solid solution [1,5]. Numerous studies have focused on designing new compositions to improve the mechanical properties of HEAs by incorporating further strengthening mechanisms such as precipitation hardening [6] and interstitial solid solution strengthening (e.g., by adding carbon) [7] besides the intrinsic substitutional solid solution strengthening.

The recent development of non-equiatomic HEAs with metastable bulk phases has introduced a more efficient way to improve strength and ductility simultaneously by triggering transformation induced plasticity (TRIP) [8,9] and/or twinning induced plasticity (TWIP) effects [7,10]. This novel metastability-engineering strategy opens up even more space for mechanism-driven HEA design owing to the tunable stability of the solid solution phases.

Although substantial research efforts have been devoted to the compositional design of HEAs, few studies have been conducted to also utilize microstructure control for tuning their mechanical properties [3,11–13]. Since the mechanical response of structural materials, such as strength, ductility and toughness, are highly sensitive to microstructure [14], it is important to understand and design specific microstructure features in close concert with the vast compositional degrees of freedom of HEAs to further broaden their mechanical property spectrum.

* Corresponding author.
** Corresponding author.
E-mail addresses: j.su@mpie.de (J. Su), zhiming.li@mpie.de (Z. Li).

https://doi.org/10.1016/j.actamat.2018.10.017
1359-6454/

In the current work, an interstitial carbon alloyed HEA (iHEA), 49.5Fe-30Mn-10Co-10Cr-0.5C (at. %), was chosen for conducting such a microstructural design study. The composition was tuned for a stacking fault energy (SFE) regime that allows joint and sequential activation of phase transformation from face-centered cubic (FCC) matrix to hexagonal close-packed (HCP) martensite and mechanical twinning during room temperature deformation [7,15]. The sequence or respectively overlap in the activation of these two effects, together with dislocation slip, depends not only on the loading scenario but also on the microstructures. More specific, both mechanisms have been reported to show strong dependence on grain size and local partitioning of the alloying elements [16,17]. According to Mahajan et al. [18,19], nucleation and growth of HCP-martensite and twins involve specific dislocation patterns and interactions at grain boundaries, formation of stacking faults and passages of Shockley partials. Grain refinement influences dislocation pile-ups in front of grain boundaries, thus setting the back stresses level. Consequently, higher external stresses are required to generate more dislocations and stacking faults. Also, nucleation of both, mechanical twins and HCP-martensite require specific configurations of stacking faults at the grain boundaries so that their frequency scales inversely with grain size [20,21]. In addition, pre-existing dislocations increase the mechanical stability of the FCC structure as they inhibit the motion of mobile dislocations and constitute effective barriers to the growth of martensite lamellae [22,23] and twins [17]. Therefore, both, grain refinement and pre-existing substructures can lead to the higher resistance to deformation-induced martensitic transformation and twinning of the FCC matrix [24–26].

Based on the characteristics of the TWIP-TRIP-assisted iHEA and the grain size effects on the phase transformation and twinning discussed above, we propose here a novel approach to improve the mechanical properties of an iHEA by hierarchical microstructure design [27–29]. Experimentally, this was achieved by means of recovery and partial recrystallization of the cold-deformed alloy. A series of bimodal and trimodal microstructures covering a wide range of grain sizes from 50 nm to tens of micrometers were developed so as to manipulate the phase stability of the FCC matrix to different levels of metastability [30,31]. In this way, HCP-martensitic transformation and twinning can be expanded to larger strain domains and in smaller scales upon deformation. As a consequence, the work hardening rate is expected to be enhanced, which, in turn, gives rise to the improved ductility and tensile strength. The systematic investigation is conducted to fundamentally understand the effects of grain-structure hierarchy on deformation mechanisms, work hardening behavior and final mechanical properties of the iHEA. The new insights obtained from merging synergetic effects from both, compositional and microstructural tuning can serve as an important guidance for future developments of advanced HEAs with superior mechanical properties.

2. Experiment

The iHEA used in the present study has a nominal composition of 49.5Fe-30Mn-10Co-10Cr-0.5C (at. %). The chemical composition measured by inductively coupled plasma (ICP) mass spectrometry is listed in Table 1. Hot rolling was performed on the as-cast alloy at 900 °C to a thickness reduction of 50%, followed by homogenization at 1200 °C for 2 h in an Ar atmosphere and then water quenching. The as-homogenized plate presented a single FCC structure and equiaxed grains with an average size of 65 μm. Cold-rolling was performed on the as-homogenized plates to a thickness reduction of 67%. The as-cold-rolled specimens were then subjected to tempering at 400 °C and annealing at 650 °C and 750 °C for different times to create a series of different microstructures. All the heat treatments were conducted using a dilatometer with a heating rate of 10 K/s and a cooling rate of 50 K/s which was approximately equivalent to that of water-quenching.

Table 1
Chemical composition of the iHEA measured by inductively coupled plasma mass spectrometry.

	Fe	Mn	Co	Cr	C
Concentration (at.%)	49.35	30.48	10.31	9.24	0.63

The microstructures of as-cold-rolled and heat-treated specimens were characterized in the cross-section of the rolling direction (RD) and the normal direction (ND) of the sheets, while the tensile samples were analyzed in the cross-section of the RD and the transverse direction (TD). Electron backscattered diffraction (EBSD) measurements were performed using a Jeol JSM-6500F field emission gun scanning electron microscope (SEM) equipped with a high resolution camera and a TSL-OIM data analysis software. All inverse pole figure (IPF) maps were plotted using the ND as reference axis. Electron channeling contrast (ECC) imaging was coupled with the EBSD analysis to reveal deformation substructures by a Zeiss-Merlin SEM. X-ray diffraction (XRD) measurements were performed by using a Meteor0D energy dispersive point detector with Cobalt source operated at 40 kV and 30 mA. Transmission electron microscopy (TEM) analysis was performed using a FEI-TITAN at an acceleration voltage of 300 kV. TEM thin foils were prepared by mechanical grinding followed by electro-polishing with a solution of 5% perchloric acid in acetic acid.

Regular dog-bone shaped tensile samples with a thickness of 1 mm were machined from the alloy sheets by electron discharge machining. The total length of the specimen is 20 mm, and the gauge length and width are 4 mm and 2 mm, respectively. Room temperature tensile tests were conducted at a constant speed of 4 μm/s which is equivalent to a strain rate of 0.001/s by using a Kammrath & Weiss tensile device. The macroscopic strain distribution and evolution were measured by a digital image correlation (DIC) technique with Aramis software (GOM GmbH). Nano-indentation tests were performed using a Hysitron TriboScope nano-indentation system with a Berkovich shaped indenter with a maximum load of 2500 μN.

3. Results

3.1. Microstructure of as-cold-rolled alloy

Fig. 1 presents the EBSD maps, ECC images and XRD pattern of the as-cold-rolled specimen. A large number of shear bands can be seen crossed and embedded among the flattened parent grains (e.g. Region I in Fig. 1a). Deformation during cold-rolling was highly localized in the shear bands resulting in regions with large lattice distortion beyond the resolution limit required for reliable EBSD indexing, shown as black bands in the EBSD maps (Fig. 1a–c). A dual-phase structure consisting of deformation induced HCP-martensite and FCC phase is formed (Fig. 1b). By ECC imaging, nano-grains are observed inside the shear bands mixed with nano-lamellae (Fig. 1d). Moreover, micro-shear bands with the thickness of sub-micrometers are found penetrating through the parent grains (e.g. Region II in Fig. 1a). Enlarged ECC image of the micro-shear band inside the HCP-martensite grain is displayed in Fig. 1e. The volume fraction of the HCP-phase is about twice that of the FCC phase from the quantitative XRD analysis according to the Rietvelt method (Fig. 1f). There is no BCC or BCT martensite identified by either EBSD or XRD technique.

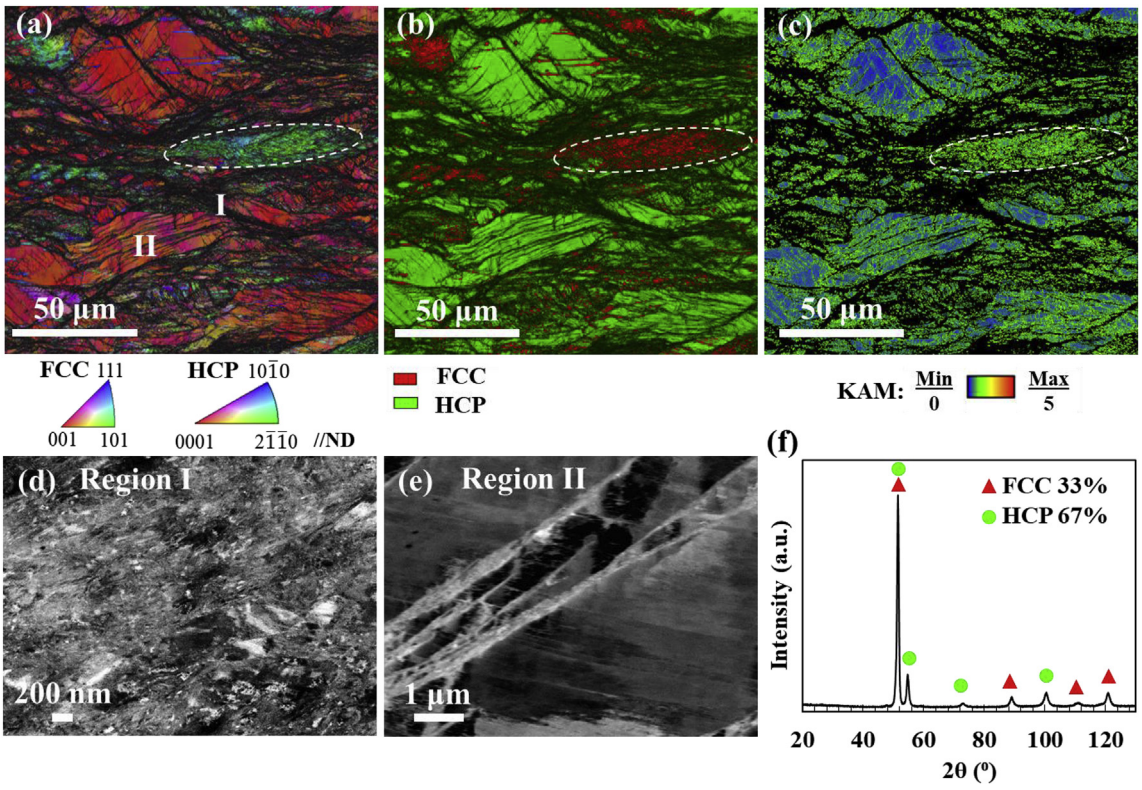

Fig. 1. Microstructure and phase analysis of as-cold-rolled specimen: (a) inverse pole figure (IPF) map superimposed with image quality (IQ) map, (b) phase map overlapped with IQ map, (c) KAM map (with a residual FCC grain circled in the dashed ellipse), (d) ECC image of region I showing nanocrystals and nano-lamellae in the shear band, (e) ECC image of region II revealing micro-shear bands in a HCP-martensite grain, and (f) XRD pattern with the volume fractions of FCC and HCP phases.

It is worth mentioning that, besides the shear-banded regions, the strain distribution in the large grains is also heterogeneous. In the kernel average misorientation (KAM) map with the 1st nearest neighbor correlation (Fig. 1c), the KAM values indicate the densities of the geometrically necessary dislocations (GNDs) [32]. It can be seen that the retained FCC grains have higher dislocation densities compared to the deformation induced HCP-martensite grains. Accordingly, the former should possess higher driving forces for subsequent recrystallization than the latter. Furthermore, HCP-martensite exhibits a near-basal texture with the {0001} direction along the ND of the as-rolled sheet, while the retained FCC phase shows a {101} fiber texture, i.e., {101}//ND and {111}//TD, in the inverse pole figure (IPF) map (Fig. 1a).

3.2. Development of bimodal microstructures via tempering

Fig. 2 reveals the microstructures of specimens tempered at 400 °C for 3 min and 10 min. Both specimens consist of a single FCC phase, indicating that deformation induced HCP-martensite reversely transformed to FCC phase during tempering (Fig. 2a_1 and b_1). At such a low temperature (~0.3T_m), no evidence of recrystallization is found. The large grains show mainly two orientation components, {101}//ND (green) and close to {111}//ND (blue and purple) in the IPF maps (Fig. 2a_2 and b_2). The {101} oriented grains (type I) correspond to the residual FCC phase as they inherited the grain orientations from the texture developed upon rolling. The {111} oriented grains (type II) are the reversely transformed FCC phase associated with the prior HCP-martensite which had a near-basal texture ({0001}//ND). This is because the reverse phase transformation from HCP to FCC upon heating is a shear transformation following the S-N relationship (i.e. $(111)_{FCC}//(0001)_{HCP}$ and $[10\bar{1}]_{FCC}//[11\bar{2}0]_{HCP}$) [33]. In addition, the retained FCC grains show higher dislocation density compared to the reversely transformed ones (see KAM map, Fig. 2b_3). The image quality (IQ) maps overlaid with the grain boundaries (Fig. 2b_4) also show that a larger number of low angle grain boundaries (LAGBs) appear in the retained FCC grains. Twins are identified mostly in the reversely transformed FCC grains (marked by red lines in the IQ maps, Fig. 2a_4 and b_4).

Fig. 3 shows the ECC images and TEM analysis of the substructures in as-tempered specimens. Nano-twins with thicknesses ranging from 10 nm to 70 nm are found in the reversely transformed FCC grains (Fig. 3b). Some of them were sized below the resolution limits of EBSD. Dislocations and stacking faults (SFs) also present in some of the large grains (Fig. 3c). In the vicinity of the shear bands, nano-sized grains can be seen (Fig. 3d). To confirm these observations, TEM bright field (BF) and dark field (DF) images are shown in Fig. 3d and e (where the dashed line separates the matrix from the shear-banded region). In the DF image, nano-grains are clearly observed in the shear bands.

The nano-indentation tests conducted on the shear bands and also in the middle of the large parent grains for reference showed a large difference in hardness values, ~7.4 GPa and ~4.5 GPa, respectively. In general, the bimodal microstructures consisting of large parent grains with pre-existing nano-twins and nano-grains in the vicinity of shear bands were produced after tempering.

3.3. Formation of trimodal microstructures during annealing

Fig. 4 reveals the partially recrystallized microstructures of the specimens subjected to annealing at 650 °C for 3 min and 10 min and 750 °C for 3 min. A single FCC phase formed for all annealing

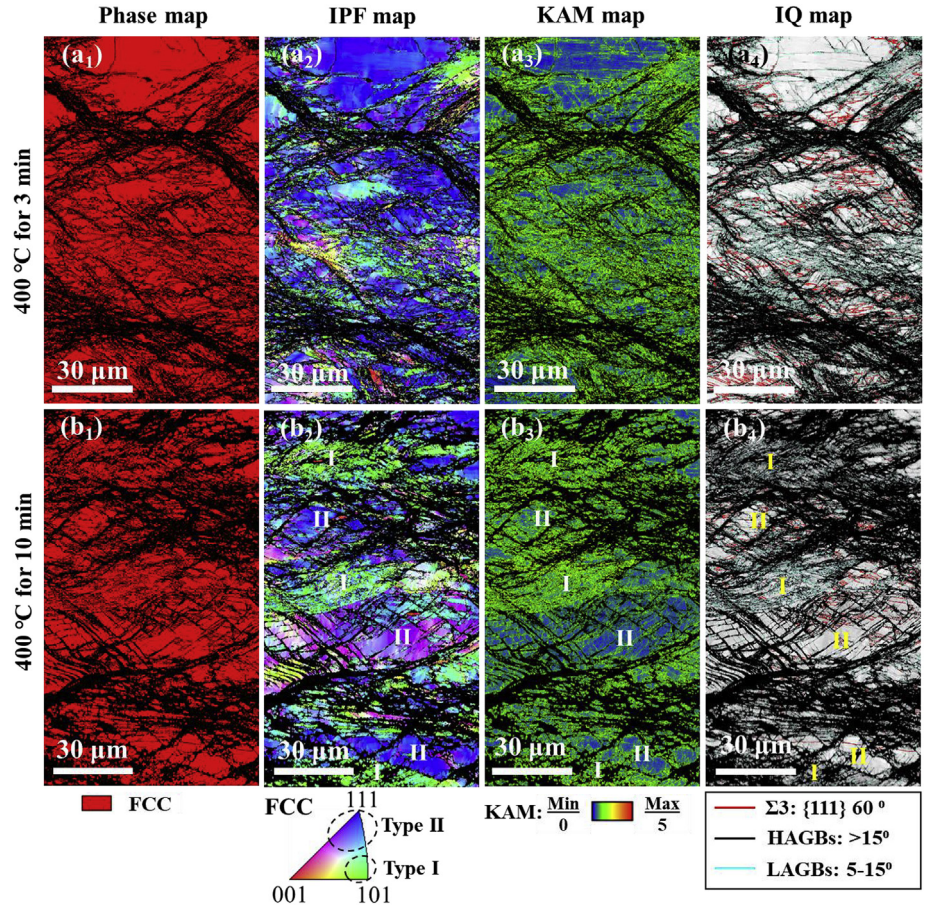

Fig. 2. Microstructures of the specimens tempered at 400 °C for (a) 3 min and (b) 10 min: (1) phase maps, (2) IPF maps, (3) KAM maps, and (4) image quality (IQ) maps superimposed with Σ3 twin and grain boundaries. Grains type I and II indicating the retained FCC phase and reversely transformed FCC phase. IPF, KAM, HAGBs and LAGBs refer to inverse pole figure, kernel average misorientation, high angle grain boundaries and low angle grain boundaries, respectively.

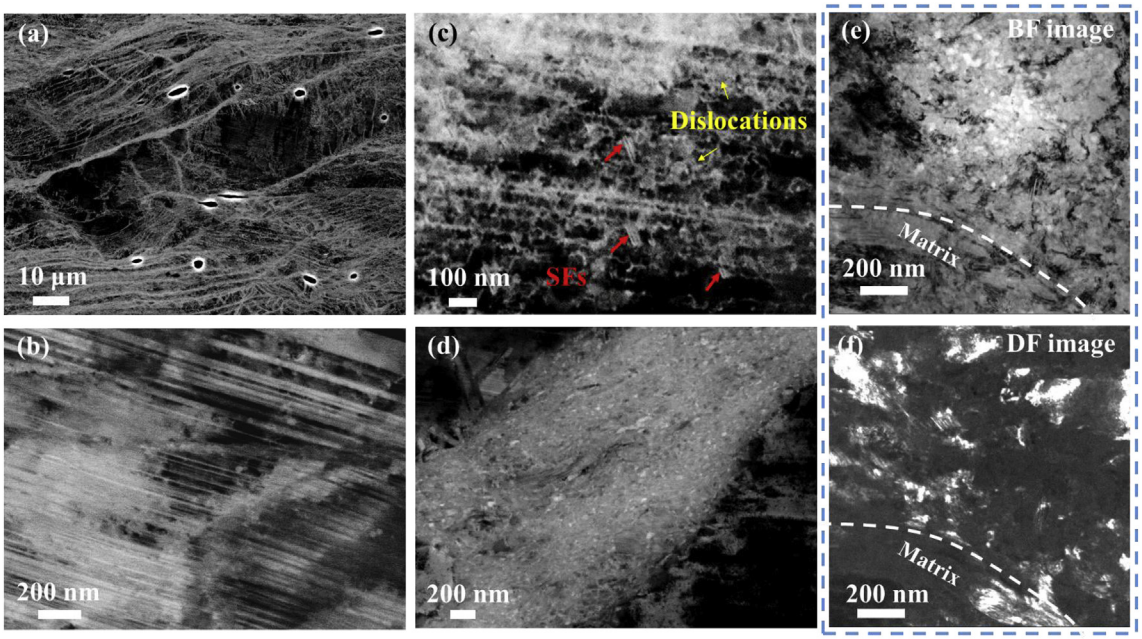

Fig. 3. ECC images of the specimens tempered at 400 °C for 3 min, (a) overview showing shear bands embedded in large parent grains, (b) nano-twins in the reversely transformed FCC grain, (c) a high density of dislocations and stacking faults (SFs) in the large grain and (d) nanocrystals in the shear band. (e) TEM bight field (BF) image and (f) dark field (DF) image revealing nano-grains formed in the shear bands.

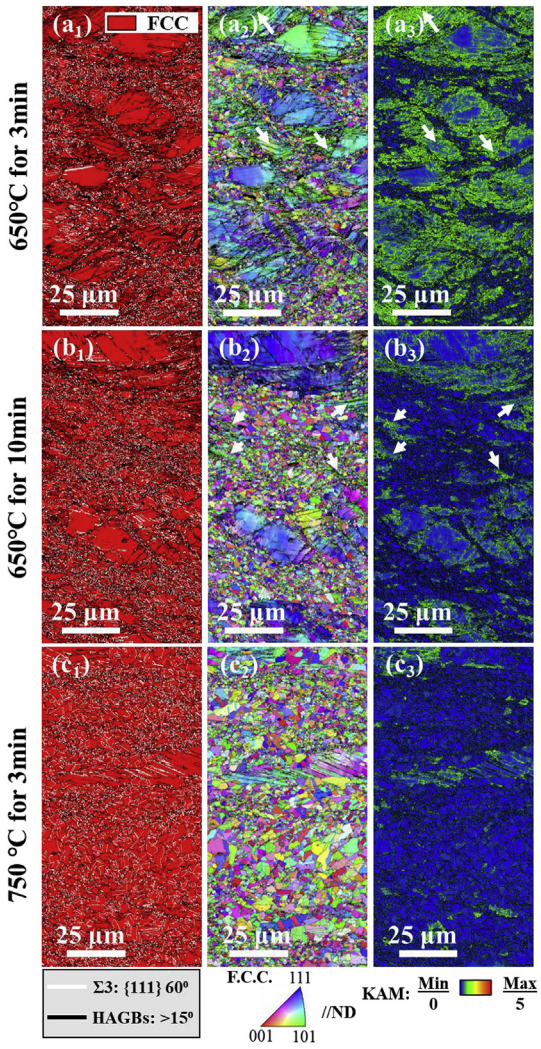

Fig. 4. Microstructures of the specimens subjected to annealing at (a) 650 °C for 3 min, (b) 650 °C for 10 min (white arrows pointing residual FCC phase) and (c) 750 °C for 3 min: (1) phase maps superimposed with Σ3 twin boundaries and HAGBs, (2) IPF maps overlaid with IQ maps and (3) KAM maps.

conditions (Fig. 4a_1, b_1 and c_1). No thermally induced HCP-martensite is observed after cooling. Statically recrystallized (SRX) dislocation-free grains form at the expense of the deformation structures (see KAM maps, Fig. 4a_3, b_3 and c_3). It can be seen that recrystallized grains preferentially nucleate in the vicinity of the shear bands in the specimen annealed at 650 °C for 3 min (Fig. 4a). With increasing the annealing time to 10 min, besides the shear-banding related recrystallization, a large portion of the retained FCC grains undergo recrystallization, as marked by the white arrows in Fig. 4b. At a higher annealing temperature of 750 °C, the volume fraction of SRX grains increases dramatically (Fig. 4c). Moreover, annealing twins form in the recrystallized grains, while much finer mechanical twins are found in the un-recrystallized grains (marked by white lines in phase maps, Fig. 4a_1, b_1 and c_1).

Fig. 5 shows the partitioned EBSD maps of the hierarchical microstructure of the specimen annealed at 650 °C for 10 min in the way of un-recrystallized grains and recrystallized grains with two different levels of sizes (medium >1 μm and small <1 μm). Most of the medium-sized recrystallized grains (1–4 μm) formed by consuming the large parent grains (Fig. 5a_2). For comparison, smaller grains with average size below 1 μm mainly nucleated in the vicinity of the shear bands. The un-recrystallized grains were segmented by micro shear-bands into smaller parts with sizes ranging from 10 to 35 μm. Overall, a trimodal microstructure was attained after annealing at 650 °C for 10 min consisting of: (i) large un-recrystallized grains with nano-twins (~45 vol %); (ii) medium-sized recrystallized grains with sizes of 1–4 μm (~33 vol %) and (iii) small recrystallized grains with sizes less than 1 μm (~22 vol %) (Fig. 5b).

The ECC image of the retained FCC grain shows blocks of deformation substructure (Fig. 5c). At higher magnification, a high density of dislocation walls is observed inside the block cells (Fig. 5d). In contrast, numerous mechanical twins with dislocations inside the twin lamellae can be seen in the reversely transformed FCC grains (Fig. 5e and f). Nano-grains are found inside the micro shear-bands with an average size of around 100 nm (Fig. 5g). Nano-carbides ($M_{23}C_6$, where M represents the substitutional elements Fe, Mn, Co and Cr [7]) are mainly observed in the recrystallized regions associated with shear bands (Fig. 5h). This is related to the highly concentrated plastic deformation in the shear bands which gives rise to locally increased defect concentrations, strain energy and dissipative heating. Thus, the diffusion rate of carbon is assumed to be higher in the shear bands, which results in the favored formation of carbides in these regions during the subsequent annealing. In addition, a higher number density of carbides is detected along the chain of the nano-grains (Fig. 5h), which indicates that such nano-particles pinned grain boundaries, preventing their motion.

3.4. Stress-strain curves and strain hardening response

The engineering stress-strain curves of the specimens subjected to tempering and annealing with different hierarchical microstructures are shown in Fig. 6a. As a comparison, the engineering stress-strain curves of the fully recrystallized microstructures with average grain sizes of 4 μm and 160 μm from preview work [7] are also presented in Fig. 6a (dash lines). The true stress-strain curves superimposed with their corresponding strain hardening plots are displayed in Fig. 6b. The yield strength, ultimate tensile strength (UTS), elongation to fracture and uniform elongation of the specimens at different conditions are summarized in Fig. 6c together with the volume fraction and the average size of SRX grains (Fig. 6d).

A high yield strength of ~1.3 GPa and a UTS of ~1.5 GPa are observed for the tempered specimens with bimodal microstructures, although the total elongation is only 12%–14%. After annealing at 650 °C for 3 min, where recrystallization mainly occurred at shear bands, a good combination of yield strength (824 MPa), UTS (1.05 GPa) and ductility (33%) is attained. As a comparison, for the specimens annealed at 750 °C for 3 min with a higher recrystallized volume fraction (85%), the ductility is substantially enhanced from 33% to 60%, yet, at sacrificing some of the yield strength which drops from 824 MPa to 555 MPa, but the UTS only slightly decreases (1050 MPa–938 MPa). These observations indicate that a more pronounced work hardening behavior appears with a larger amount of SRX grains. It is also found that not only the uniform elongation (4%–38%) but also the post-necking elongation (10%–24%) is improved with increasing the volume fraction of recrystallization from 41% to 85%. Comparing with the fully recrystallized structure with an average grain size of ~4 μm, the yield strength of the trimodal structure annealed at 750 °C increases from 485 MPa to 555 MPa, while the UTS and total elongation are at similar levels. The fine-grained material annealed at 900 °C for 3 min also showed a mixture of large grains (up to 8 μm) and smaller grains (~1 μm) [7,15]. Nevertheless, the yield strength and the UTS of the materials with trimodal microstructures

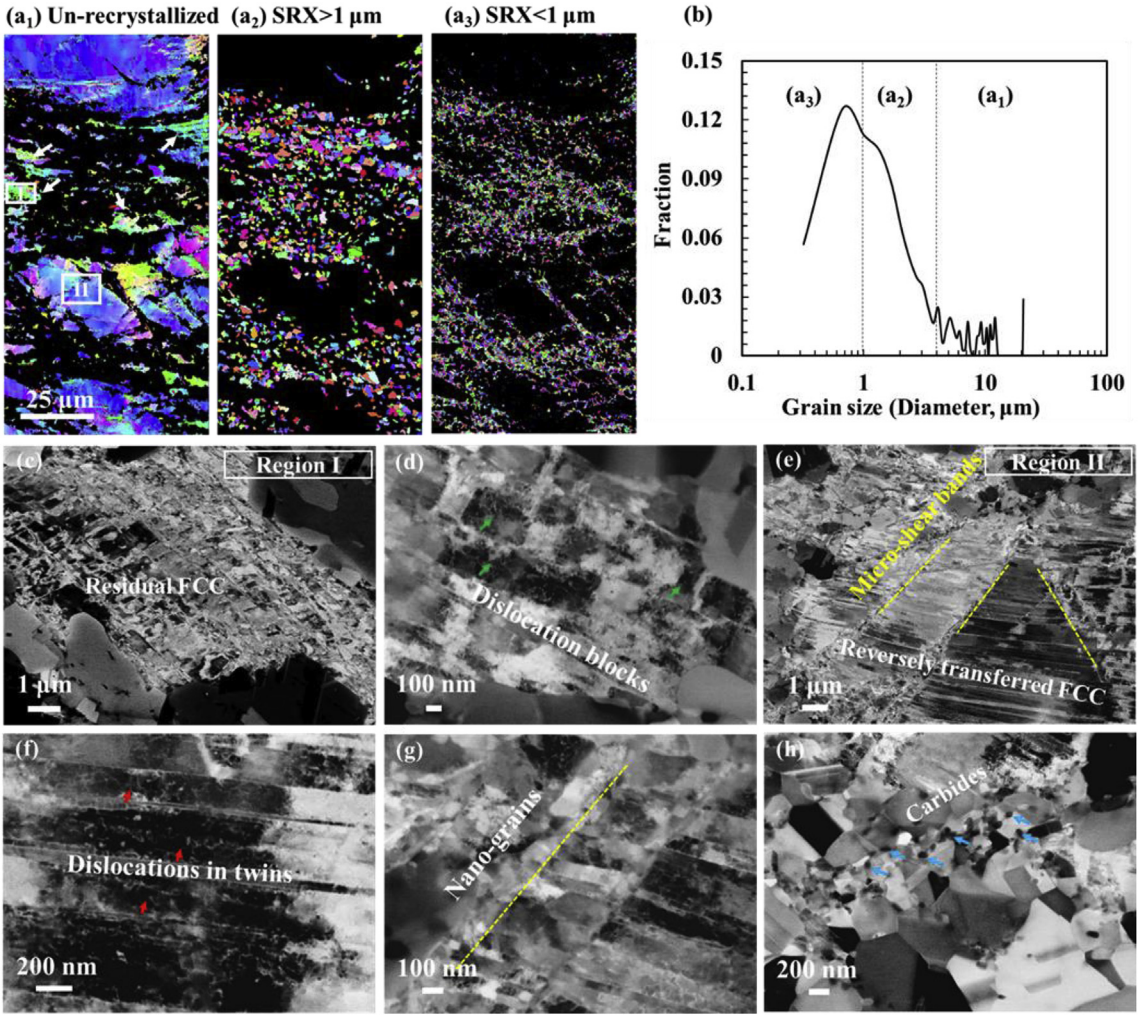

Fig. 5. Partitioned IPF maps of the specimen annealed at 650 °C for 10 min: (a_1) un-recrystallized grains, (a_2) SRX grains >1 μm, (a_3) SRX grains <1 μm and (b) grain size distribution; ECC images of (c) Region I of residual FCC grains, (d) zoomed in (c) showing dislocations blocks, (e) Region II of reversely transformed FCC grains showing micro-bands, (f) mechanical twins with dislocations inside reversely transformed FCC grains, (g) micro-bands with nano-grains and (h) nano-carbides in the recrystallized grains in the vicinity of the shear bands.

annealed at 750 °C are substantially enhanced compared to those of specimens with uniform coarse-grained structure (~160 μm) and their ductility is slightly improved.

The work hardening rate of the tempered samples decreases linearly with true strain until necking, while a multi-stage strain hardening response appears in the annealed specimens with tri-modal grain structures. Specifically, the specimens subjected to annealing at 650 °C (≤ 55% SRX) show three-stage work hardening behavior, while the specimens annealed at 750 °C (≥ 85% SRX) present clearly four stages of strain hardening with a sudden increase of the work hardening rate at early strains (2–5%).

3.5. Microstructure evolution upon deformation

To correlate the work hardening behavior with the underlying deformation mechanisms upon uniaxial tensile loading, the microstructural evolution of two different hierarchical grain structures (650 °C for 3 min and 750 °C for 3 min) are compared for a range of local strains (3%–45%). It should be noted that the recrystallized volume fraction of the former material (650 °C) is 50% smaller than that of the latter one (750 °C). In the grain size distribution map (Fig. 7c), it can be seen that the volume fraction of small grains (<1 μm) of the specimen annealed at 650 °C is higher than that of the sample subjected to annealing at 750 °C, but the medium-sized recrystallized grains (1–6 μm) in the former is less than that in the latter. At a low strain of 3%, HCP-martensite lamellae are only found in the large parent grains in the specimen annealed at 650 °C, but in both parent grains and medium-sized recrystallized grains in the sample annealed at 750 °C according to EBSD analysis (Fig. 7a and b). The fraction of the HCP-martensite of the former (~0.2 vol %) is also lower than that of the latter (~0.5 vol %). In the large parent grains, the HCP-martensite lamellae are found along the pre-existing twin boundaries (as shown in the enlarged IQ map, Fig. 7d).

ECC imaging was applied to analyze the formation of HCP-martensite lamellae and twins at submicron scales. In the specimens annealed at 750 °C for 3 min, numerous fine HCP-lamellae and twins are observed in the medium-sized recrystallized grains and most of them penetrate the entire grain (Fig. 8a). Multiple variants of HCP-martensite or twinning systems are activated in the grain with orientation {101}//ND (marked by the black rectangular in the IPF map, Fig. 7b_1). In the recrystallized grains, incoherent annealing twin boundaries (showing facets) also serve as nucleation sites for HCP-martensite and twins (Fig. 8b). The thickness of

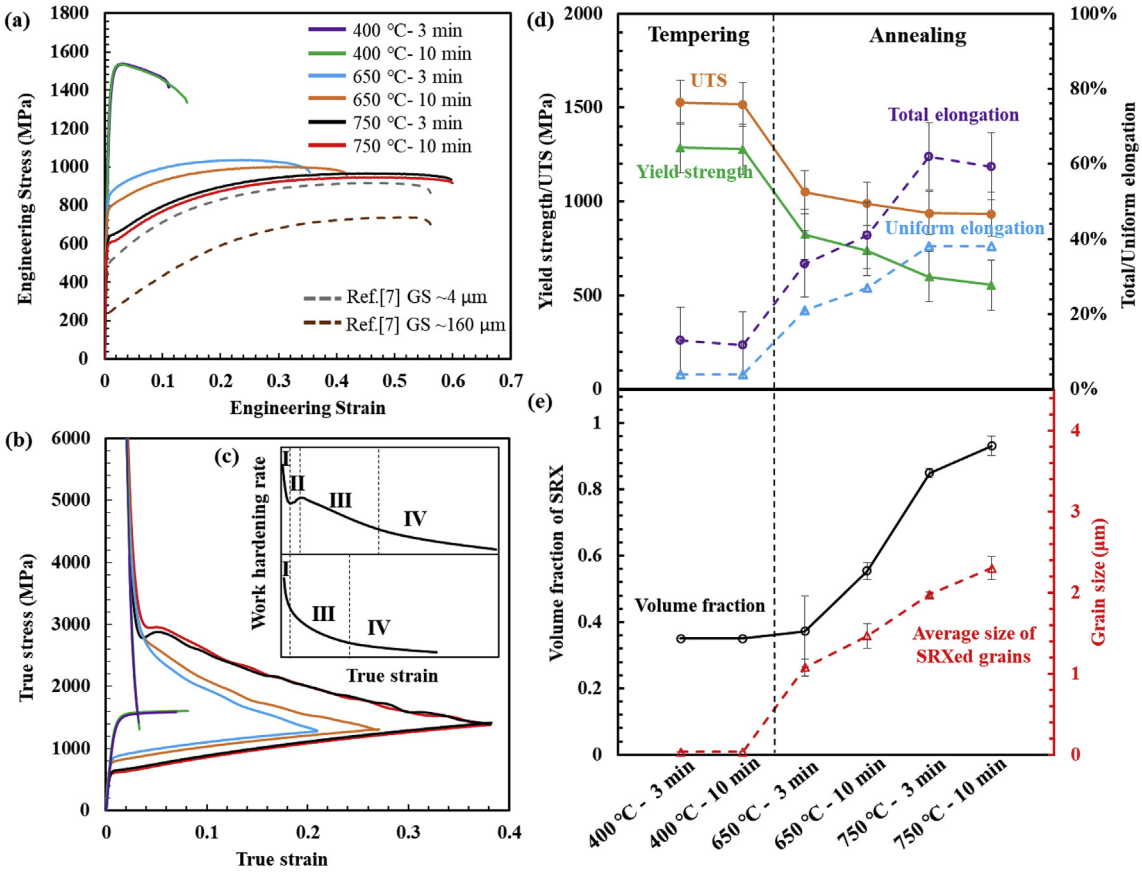

Fig. 6. (a) Engineering stress-strain curves of the specimens heat-treated at 400 °C, 650 °C and 750 °C for 3 min and 10 min. The two dash-lines represent the stress-strain curves of the fully recrystallized grain structures with average grain sizes of ~4 μm and 160 μm from Ref. [7]. (b) true stress-strain curves superimposed with the corresponding strain hardening curves, (c) illustration of two different work hardening behavior at 750 °C (upper) and 650 °C (lower), (d) summary of yield strength, UTS, total elongation and uniform elongation and (e) volume fraction and average size of SRXed grains in the specimens at different heat treatment conditions. For the tempered specimens, the volume fraction of nano-grains were considered as the fraction of shear bands.

HCP-martensite and twin lamellae at this stage was very thin, viz. below the EBSD resolution limit. In the ultrafine recrystallized grains with size below 500 nm (Fig. 8c), stacking faults and partial dislocations can be seen near grain boundaries. In the large parent grains, besides the martensite growing along the pre-existing twinning plane, partial dislocations and thin martensite lamellae are observed inclining at mainly two sets of angles (i.e., 35–40° and 90°) to the pre-existing twin boundaries (marked by red arrows in Fig. 8d). In the specimen annealed at 650 °C for 3 min, stacking faults and partial dislocations are found in the large parent grains and they are blocked by the pre-existing dislocation substructures (Fig. 8e and f).

To demonstrate the effect of grain size on the formation of HCP-martensite during deformation, the microstructures of the specimen annealed at 750 °C for 3 min at local strains of 10% and 30% are shown in Fig. 9. At a local strain of 10% (Fig. 9a_2), a higher fraction of HCP-martensite with larger thickness is detected in both parent grains and medium-sized recrystallized grains compared to those at the strain of 3% (2 vol % vs. 0.5 vol %). Moreover, higher KAM values are found along grain boundaries, particularly concentrated in the region of small SRX grains (<1 μm). This is attributed to the strong interactions of dislocations with grain boundaries and formation of stacking faults in front of the boundaries. Annealing twin boundaries are also strong obstacles for dislocation movement. The reactions of dislocations with twins lead to the transition of twin boundaries to random high angle grain boundaries (HAGBs) partially (see white arrows in Fig. 9c). With increasing the local strain to 30% (Fig. 9b_2), the overall volume fraction of HCP-martensite largely increases (8 vol %) and the martensite lamellae in the small recrystallized grains (~1 μm) are thick enough to be detected by EBSD.

At a high local strain of 45%, exceeding the global uniform elongation value, some of the large parent grains are found mostly transformed to HCP-martensite in the specimen annealed at 750 °C for 3 min (Fig. 10a). The HCP phase shows a lower dislocation density than the FCC matrix. In the specimen annealed at 650 °C for 10 min, the volume fraction of deformation induced HCP-martensite (13 vol %) is much lower than that in the specimen annealed at 750 °C for 3 min (33 vol %) at the same local strain (Fig. 10b). This is mainly due to the inhibition of the growth of martensite plates by pre-existing twin boundaries in the large parent grains in the former material.

4. Discussion

4.1. Formation of hierarchical microstructures

A schematic plot of creating hierarchical microstructures through thermomechanical processing (from homogenization to cold rolling to tempering/annealing) is shown in Fig. 11. The as-homogenized materials had an equiaxed recrystallized microstructure with a single FCC phase. Upon cold rolling, deformation induced HCP-martensite formed with retained FCC matrix leading to a dual-phase microstructure and severe shear bands appeared

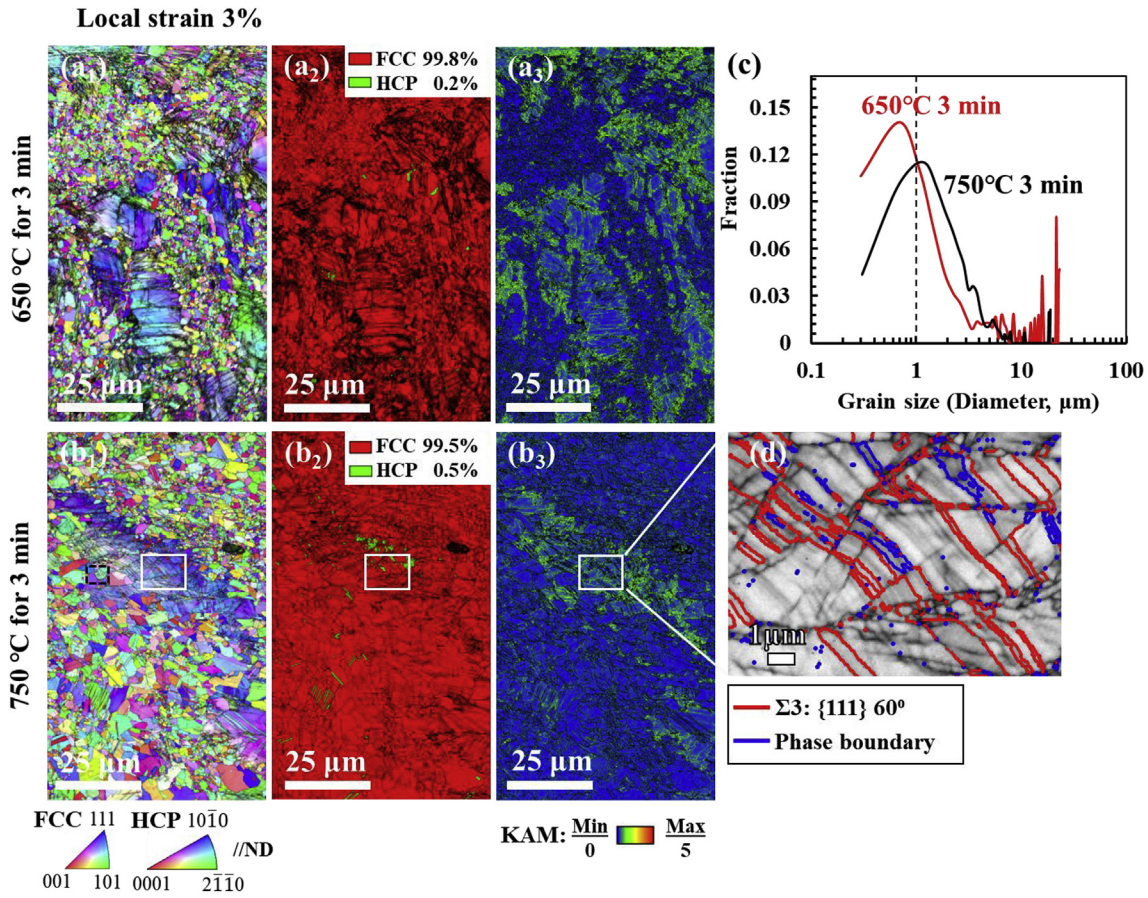

Fig. 7. Microstructures at a local strain of 3%: (1) IPF map, (2) phase map and (3) KAM map of the specimens annealed at (a) 650 °C for 3 min and (b) 750 °C for 3 min, (c) comparison of the grain size distributions of the two specimens before tensile loading, and (d) the enlarged IQ map of the rectangular region in (b) showing Σ3-twin boundaries and phase boundaries.

upon deformation to 67% which is equivalent to a true strain of 1.1. When the as-rolled sheet was subjected to heat treatment at and above 400 °C, deformation induced HCP-martensite reversely transformed to FCC matrix through displacive transformation following the S-N relationship [33], while twins which co-existed with martensite lamellae prevailed in the parent grains. After tempering at 400 °C for short times (3 min and 10 min), recovery was dominant in the large parent grains and nano-grains remained in the shear bands. Thus, single-phase bimodal microstructures consisting of large unrecrystallized grains with pre-existing nano-twins and nano-grains in the vicinity of the shear bands were produced.

During annealing, static recrystallization took place particularly in the vicinity of shear bands due to their largely concentrated deformation and the higher density of dislocations. Nano-grains also appeared as the precursors for recrystallization, and thus no incubation time was required and more nucleation sites were available for recrystallization. As a consequence, the recrystallization kinetics of the shear bands was much higher and the size of the recrystallized grains was finer compared to those of the large parent grains. In the residual FCC grains, cell blocks appeared with dense dislocation walls (DDWs). This was also observed in other FCC metals, such as in Ni subjected to large strain cold-rolling [34], and in Fe-22Mn-0.6C (wt.%) steel [26] and 40Fe40Mn10Co10Cr HEA [10] upon tensile testing. Cell blocks are formed by activating multiple slip systems simultaneously and they are separated by dislocation boundaries that are geometrically necessary [34]. Deng et al. [10] showed that in a single FCC phase twinning-assisted HEA, 8 slip systems can be equally stressed in the grains with the orientation of <001> along the tensile direction. This is due to the fact that these slip systems have the same Schmid factor which is higher than that for mechanical twinning. Therefore, the retained FCC grains showed a preferred orientation of (110)//ND and (100)// RD together with dense dislocation cell structures. On the contrary, the reversely transformed FCC phase contained multiple nano-twins. Also, in regions adjacent to the shear bands and the micro-shear bands, the dislocation density was higher (KAM values of 1–2) compared to those in the grain interiors (KAM<1) (Fig. 4a_3 and b_3). This observation was related to the highly localized deformation created by shear banding where the crystals adjoining to the shear bands rotated and formed GNDs to accommodate strains which caused a local increase in the misorientation as reflected by the KAM values [35,36]. As such, both the retained and reversely transformed parent grains recrystallized through the formation of LAGBs and rotation and coalescence of subgrains. Yet, the recrystallization kinetics of the retained FCC grains was higher than that of the reverted ones due to the higher dislocation densities in the former. In this way, trimodal grain structures were produced characterized by small recrystallized grains associated with shear bands, medium-sized grain recrystallized from parent grains and unrecrystallized large grains.

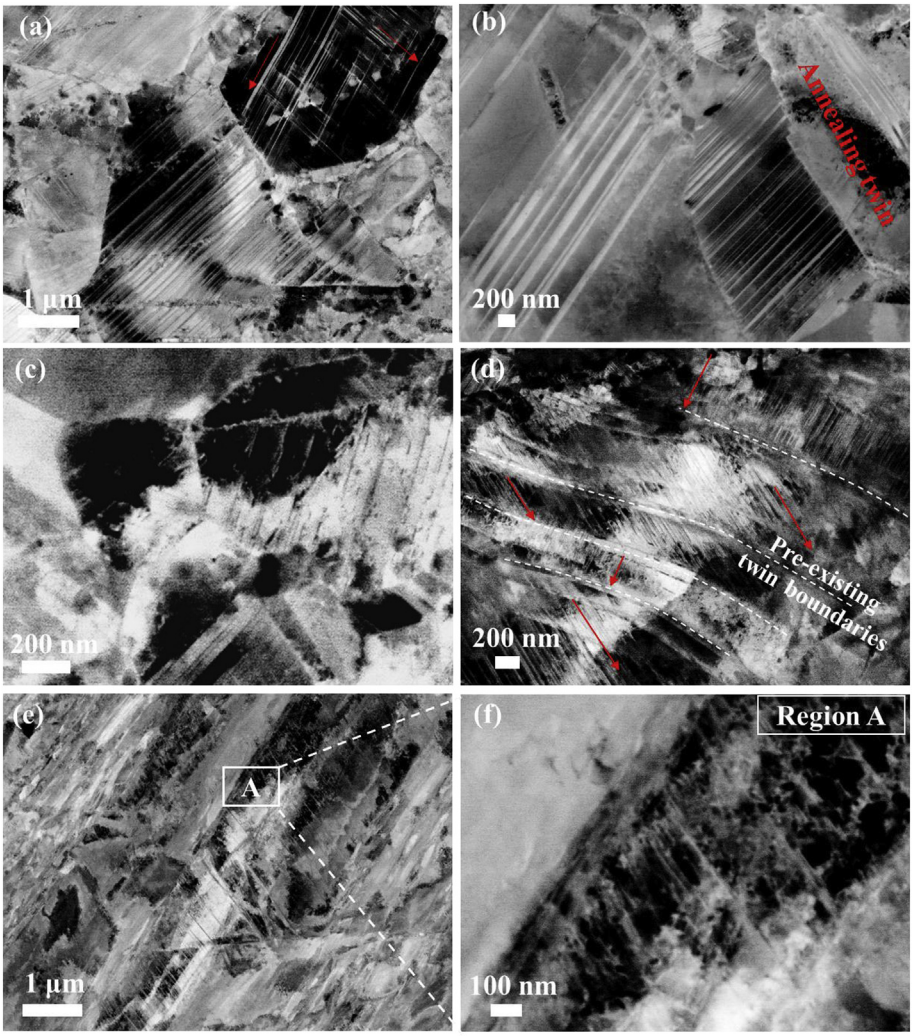

Fig. 8. ECC images of the specimen annealed at 750 °C for 3 min at a local strains of 3%: (a) HCP-martensite lamellae formed in medium sized recrystallized grains, (b) HCP-martensite formed in front of the incoherent annealing twin boundaries, (c) stacking faults in ultrafine grains (with grain size <500 nm), (d) partial dislocations and fine martensite lamellae in large parent grains with pre-existing twins. ECC images of the specimen annealed at 650 °C for 3 min at the same strain: (e) the deformation substructure in the large grains and (f) zoomed in image showing stacking faults and partial dislocations blocked by dislocation substructures.

4.2. Improvement in yield strength through hierarchical microstructures

The specimens subjected to tempering at 400 °C with bimodal microstructures exhibited much higher yield strength compared to those annealed at the higher temperatures. This is mainly attributed to the pre-existing nano-twins and dislocations in the large parent grains and nano-grains remained in the shear bands. Therefore, the yield strength can be considered as the summation of the strength contributions from twin boundaries, dislocations and grain refinement, written by equation (1) with the rule of the mixture [37]:

$$\sigma^{y} = \sigma^{i} + f^{TW}\Delta\sigma^{TW} + f^{DIS}\Delta\sigma^{DIS} + f^{GR}\Delta\sigma^{GR} \quad (1)$$

where σ^{i} is the initial yield strength of the current iHEA with the average grain size of 65 μm. The terms indicated by f represent the volume fraction of the grains associated with different microstructural features, such as pre-existing nano-twin boundaries (TW), dislocations (DIS) and grain refinement (GR) by nano-grains or static recrystallization, and $\Delta\sigma$ refers to the increase of the yield strength caused by each strengthening mechanism.

It is well-known that the yield strength can be improved by grain refinement which is expressed as the Hall-Petch relation [38], equation (2).

$$\Delta\sigma^{GR} = k_y\left(d^{-\frac{1}{2}} - d_i^{-\frac{1}{2}}\right) \quad (2)$$

Here, k_y is the strengthening coefficient by grain refinement and d is the average grain diameter. By plotting the Hall-Petch relation in a large range of grain sizes from 2.2 μm to 160 μm (data extracted from current and previous work [7]), the values of k_y (573 MPa·μm$^{-1/2}$) and σ_0 (179 MPa) were derived. The strengthening coefficient k_y in this case is consistent with those reported in the Fe-Ni-Co-Al-Cr HEAs with and without the addition of carbon (574 and 534 MPa·μm$^{1/2}$) [39] and the equiatomic Co-Cr-Fe-Mn-Ni HEA (494 MPa·μm$^{1/2}$) [40], but it is much higher than that stated in Fe-Mn steels (365 MPa·μm$^{1/2}$) [37]. The volume fraction of recrystallized grains, f^{SRX}, was measured from EBSD analysis according to the grain orientation spread (GOS) of which the dislocation-free recrystallized grains were less than 1°.

Upon annealing, the large parent grains underwent recovery where dislocation dipoles with opposite sign annihilated, thus the

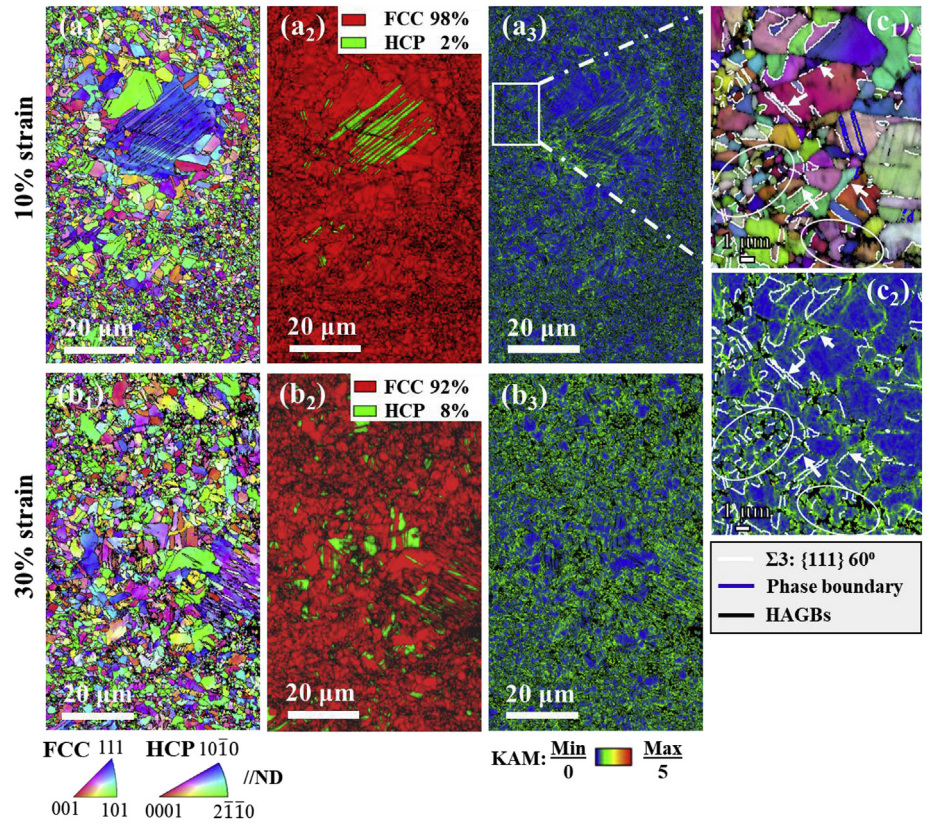

Fig. 9. IPF map, phase map superimposed with IQ map and KAM map of the specimen annealed at 750 °C for 3 min at local strains of (a) 10% and (b) 30% and (c) Enlarged map of the rectangular region. Twin boundaries pointed by white arrows and small grains circled by the ellipses.

density of retained statistically stored dislocations (SSD) was expected to be very low. The increase in yield strength owing to the pre-existing dislocations, therefore, was mainly due to GNDs which form arrays of subgrains with small misorientations. The density of GNDs (ρ_{GNDs}) can be expressed as a function of the misorientation angle (θ) and the unit length (u) [32,41].

$$\rho_{GNDs} = 2\theta/ub \tag{3}$$

where b is the magnitude of the Burgers vector (2.55×10^{-10} m) of the FCC phase. Taking $u = 10^{-5}$ m, the density of the GNDs in the annealed samples was then estimated to be around $10^{14}/m^2$ [42]. The contribution of the GNDs to the yield strength can be considered by using Taylor hardening law [43]:

$$\Delta\sigma^{DIS} = M\alpha Gb\sqrt{\rho_{GNDs}} \tag{4}$$

Here, M is the Taylor factor (3.06), α is a constant (0.2) and G is the shear modulus which was determined to be 76 GPa for this iHEA as measured by impulse excitation technique. The fractions of the GNDs of $10^{14}/m^2$ (KAM values above 1) were obtained from the KAM plots [44,45].

With knowing the contribution of grain refinement and dislocations to the yield strength, the role of pre-existing nano-twins was able to be derived. It was reported that the yield strength was related to the twin spacing, described by the twinning Hall-Petch relation (equation (5)) [26].

$$\Delta\sigma^{Twin} = k_t\lambda^{-1/2} \tag{5}$$

where λ is twin spacing and k_t is the strengthening factor by twin boundaries. Fig. 12 shows the ECC images of twins in annealed specimens. It can be seen that twin spacing became broader at higher annealing temperatures due to the migration of twin boundaries by the movement of Shorkley partials. The volume fraction of the grains with nano-twins was assumed to be the fraction of un-recrystallized and yet reversely transformed FCC grains. The dependence of the increase in the yield strength due to the nano-twins, $\Delta\sigma^{TW}$, with average twin spacing was then plotted in Fig. 11d together with the grain size Hall-Petch relation. The derived strengthening coefficient of nano-twins, k_t (195 MPa·$\mu m^{1/2}$) was much smaller than the grain boundary strengthening coefficient. The similar phenomenon was also reported in a Fe-Mn steel with pre-existing nano-twins produced by dynamic plastic deformation and subsequent annealing [37]. This indicates that nano-twin boundaries did not act as effective obstacles as the high angle grain boundaries for dislocation transmissions. The pre-existing twin boundaries had two-fold effects. At first, the coherent twin boundaries on the (111) plane provide glide plane for partial dislocations where the slip plane and the Burgers vector are parallel to the twin boundaries which help to facilitate HCP-martensitic transformation and twinning [14]. Secondly, some of the twin boundaries block the motions of dislocations as grain boundaries. When the incoming dislocations interact with twin boundaries, they either dissociate into partials along the twins or transfer through the twins depending on the nature of the dislocations and the stress state [37]. In this case, the pre-existing twin boundaries show an angle with respect to the slip planes (Fig. 8d) [37].

For the tempered samples, the augmentation of the yield stress due to nano-twins can be calculated by extrapolating the plot of the twinning Hall-Petch relation. It was found that the increase of the yield strength due to nano-twins and dislocations were around 468

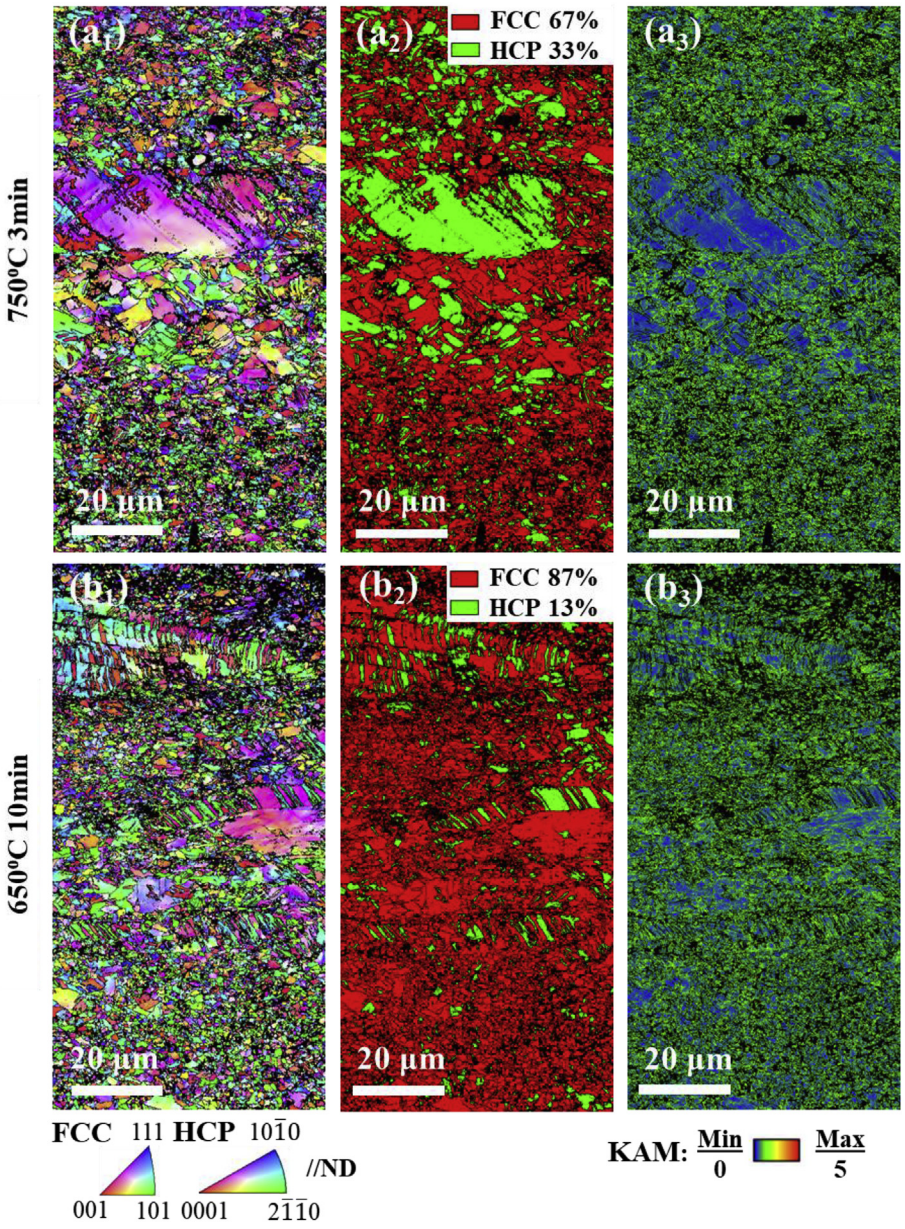

Fig. 10. IPF maps, phase maps and KAM maps at a local strains of 45% of the specimens annealed at (a) 750 °C for 3 min and (b) 650 °C for 10 min.

and 57 MPa, respectively. Hence, the shear-banded microstructure contributed about 522 MPa of the yield strength. Given that the volume fraction of the shear bands was about 35%, a yield strength of 1.5 GPa could be achieved in the nanostructures in the shear bands. A ratio of the yield strength of the nanostructures in the shear bands with respect to the large grains with nano-twins was around 1.66, which is consistent with the nano-indentation results (7.4 GPa/4.5 GPa). The contributions of nano-twins, dislocations and grain refinement to the increase of yield strength were summarized in Fig. 12e. It can be seen that the nanostructures in the shear bands and the pre-existing nano-twins in the parent grains made the primary contributions to the improvement in the yield strength of the bimodal microstructures created by tempering. In the annealed specimens with trimodal grain structures, nano-twins in the unrecrystallized grains played a larger role to the increase of the yield strength than the grain refinement by recrystallization.

4.3. Multiple strain hardening stages associated with the hierarchical microstructures

In the following, we discuss the correlation of the work hardening behavior and the strength-ductility synergy with the formation of HCP-martensite and twinning in the hierarchical microstructures. According to the models proposed by Mahajan et al. for HCP-martensite [18] and twinning [19], a normal stress of 531 MPa was required for activating both mechanisms with assuming the stacking fault energy of 18 mJ/m^2 in the current iHEA (see appendix). This critical stress was lower than the actual yield strength of all the tempered and annealed specimens.

The tempered specimens with bimodal microstructures showed an almost linear decrease of the work hardening rate until necking. Since both, the pre-deformation substructures and the nano-grains largely increased the stability of the FCC matrix, formation of HCP-martensite and mechanical twinning were inhibited to some

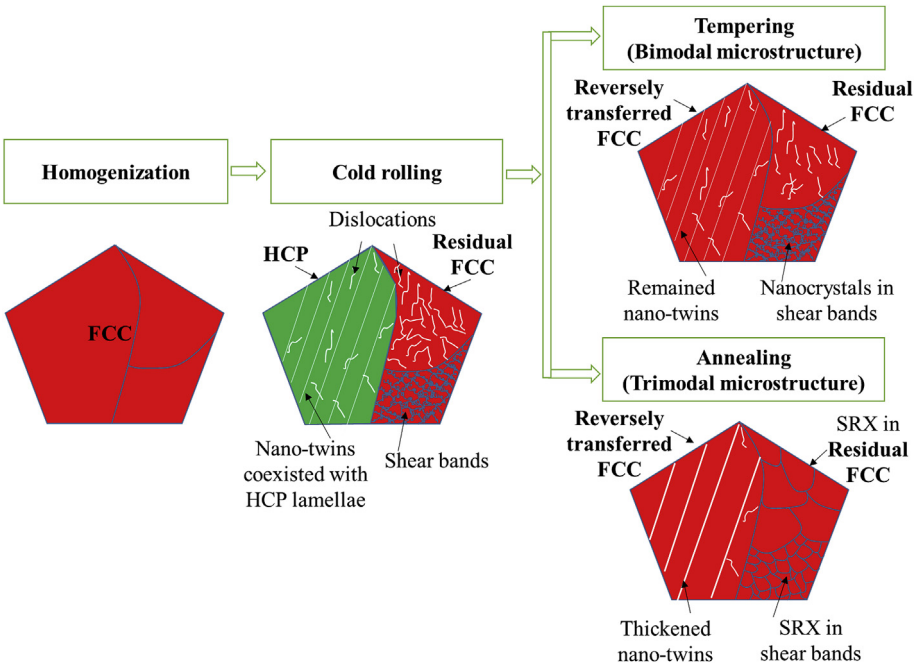

Fig. 11. Schematic plot of producing bimodal and trimodal microstructures by thermomechanical processing (homogenization-cold rolling-tempering and annealing).

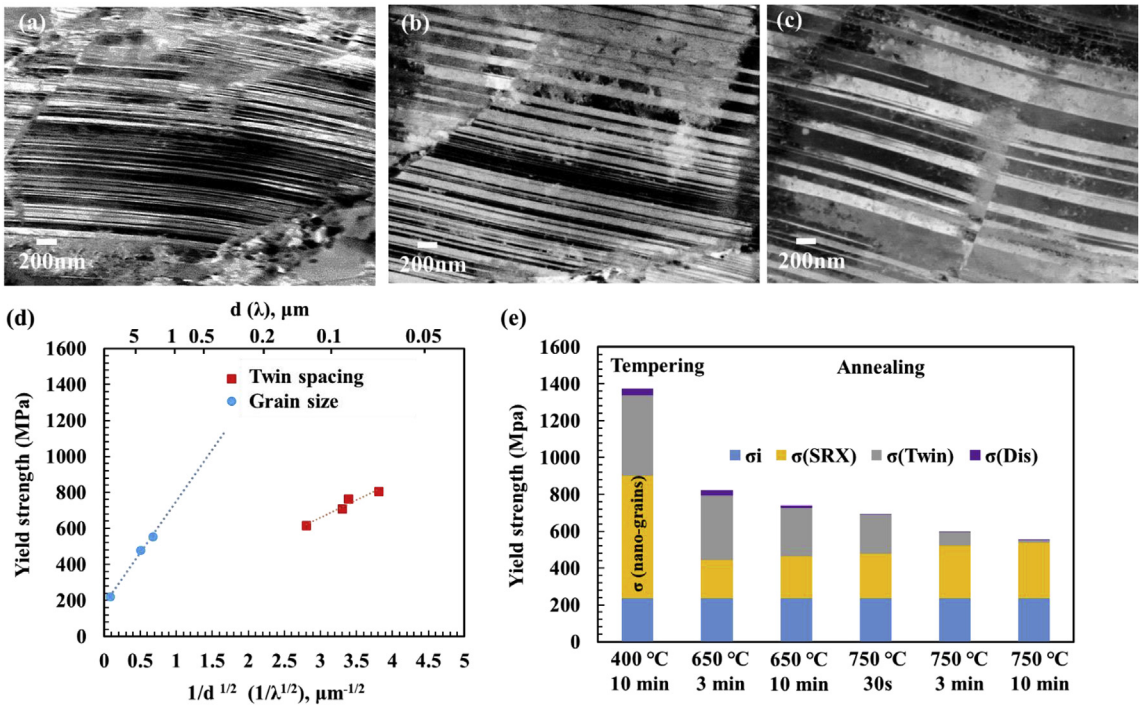

Fig. 12. ECC images showing nano-twins in specimens annealed at (a) 650 °C for 3 min, (b) 650 °C for 10 min and (c) 750 °C for 3 min, (d) Relations of the increase of the yield strength with grain size and twin spacing of the annealed specimens and (e) increase of the yield strength due to nano-grains, SRX, twins and dislocations of the specimens subjected to tempering and annealing.

extent. Plastic deformation was, hence, achieved mainly by dislocation slip and led to localized deformation. According to the Considère criterion, plastic instability is reached when the work-hardening rate is surpassed by the true stress, $\partial\sigma/\partial\varepsilon \leq \sigma$ [46]. Therefore, in the tempered specimens, the work-hardening rate was not sufficiently high to prevent early necking resulting in the limited uniform elongation.

Interestingly, the annealed samples with trimodal microstructures exhibited multistage work hardening behavior (see the schematic plot in Fig. 6c). In the first stage, the work hardening rate continuously decreased in all specimens, which is related to the rearrangement of the dislocations [26]. At higher strains, it was found that the different types of trimodal grain structures probed in this study showed a more complex, viz., multistep work hardening

response. Specifically, specimens annealed at 650 °C went through three stages of strain hardening whereas four-stage work hardening behavior appeared in the specimens annealed at 750 °C with a sudden increase at low strains (2–5%, stage II) (Fig. 7c). This is attributed to the difference in the volume fraction of recrystallized grains in the former case (55 vol %) opposed to the latter one (85 vol %). Accordingly, the latter case involves a higher amount of medium-sized recrystallized grains (1–6 μm) (Fig. 7c) which have relatively low phase stability relative to smaller crystals. Therefore, the rapid increase of the work hardening rate in stage II was ascribed to the nucleation of HCP-martensite lamellae and nano-twins in the medium-sized recrystallized grains in the specimens annealed at 750 °C. Although the volume fractions of the HCP-martensite and twins were fairly low at early strains, it was noticed that the thicknesses of such lamellae were very thin (a few nm to 100 nm) which greatly refined the microstructure, thus reducing the mean free path of dislocations, an effect known as dynamic Hall-Petch effect [26]. It was also reported that thinner twins could promote dislocation-twin interactions and leave more space for dislocation storage resulting in more pronounced work hardening [14]. In this case, both martensite lamellae and twins served as obstacles for dislocation glide. On the contrary, in the specimens annealed at 650 °C, the pre-existing dislocations trapped free mobile dislocations and the smaller grain size increased the back stresses which also affected dislocation motion. Both effects impeded formation of stacking faults. Therefore, nucleation of HCP-martensite and twins in the specimens annealed at 650 °C was sluggish at low strains and no obvious increase in strain hardening was observed in this regime.

The strain hardening in stages III and IV of all annealed specimens showed a similar trend characterized by the further decline in the work hardening rate, however, with a lower decreasing slope at the last stage. For the specimen annealed at 750 °C, the nucleation rate of HCP-martensite and twin lamellae in stage III was lower compared to that in stage II. The reason for this effect is that when the critical stresses for nucleation of HCP-martensite and twins were reached, growth rather than nucleation of such lamellae prevails. Therefore, the further decrease of the mean free path for dislocations by such lamellae was modest, reducing work hardening. Stage IV occurred roughly at strains of 10%, 12% and 18% for the specimens annealed at 650 °C for 3 min, and 10 min and 750 °C for 3 min, respectively, corresponding to a similar true stress level of around 1100 MPa. It is related to the nucleation and growth of HCP-martensite and twins in the ultrafine SRX grains since higher stresses are required to nucleate twins and/or HCP-martensite under such spatially confined conditions [18–21]. Rahman et al. [17] reported that the critical shear stress to initiate twins in a Fe–15Mn–2Al–2Si–0.7C steel increased from 62 MPa to 316 MPa with decreasing grain size from 84 μm to 0.7 μm which followed a Hall-Petch type relationship. Yoo et al. [16] found that the critical stored energy for the formation of the strain-induced martensite in an austenitic steel increased from 5.5 J/g to 9 J/g with decreasing grain size from 2 μm to 300 nm and the volume fraction of martensite reduced in smaller grains. These findings are consistent with the current observations, and hence, the true stress of ~1100 MPa is correlated to the critical stress required to grow HCP-martensite and twins in sub-micrometer sized grains. Therefore, due to the wide variation in the phase stability promoted by trimodal grain structures, the TRIP and TWIP effects were stimulated successively in grains with different sizes. Through such utilization of the size and substructure dependence of the TRIP and TWIP effects we expanded the work hardening rate into a sequence of distinct and successive mechanism regimes, enhancing the materials' strength-ductility ranges. Overall, it is thus shown that different types of hierarchical microstructures, including grains of difference size, texture, softening stage and substructure, can significantly affect the deformation modes and the associated work hardening response in such metastable HEAs, enabling tuning them for different types of strength-ductility profiles.

As discussed above, a large spectrum of mechanical properties with the yield strength ranging from 555 MPa to 1.3 GPa, UTS from 930 MPa to 1.5 GPa and total elongation from 60% to 14% was achieved through the hierarchical microstructural design. The combinations of strength and ductility reported here covered properties ranging from the strong maraging steels [47] to the ductile TRIP and TWIP steels [24,48]. Here this was achieved in a carbon interstitial HEA with well-tuned stacking fault energy coupling with hierarchical microstructures introduced by conventional thermomechanical processing. The current study not only revealed the fundamentals of the processing-microstructure-properties relationship of the iHEA but also pointed out the importance of designing microstructures that take advantage of the wide compositional degrees of freedom of HEAs for future composition and microstructure-sensitive alloy development strategies.

5. Conclusions

In this work, we presented systematic investigations on hierarchical microstructural design and the corresponding mechanical properties of an interstitial carbon alloyed high-entropy alloy ($Fe_{50}Mn_{30}Co_{10}Cr_{10}C_{0.5}$, at. %) showing joint activation of martensitic phase transformation and mechanical twinning upon loading. The main conclusions are:

A hierarchical microstructural design strategy was successfully employed to enhance the mechanical properties of an interstitial TRIP-TWIP-assisted HEA. The fundamental principle is to introduce several grain classes of different size, softening stage, texture and substructure which individually influence the mechanical stability of the FCC matrix. This effect was used to tune the local onset of phase transformation and mechanical twinning over much larger strain domains, enabling to realize and utilize a likewise wide spread of the associated strain hardening stages, ideally resulting in multistage work hardening.

Upon tempering and annealing, HCP-martensite transformed reversely to FCC matrix, whereas the mechanical twins that had co-existed with martensite lamellae prevailed in the parent grains. In the tempered specimens, bimodal microstructures were produced consisting of nano-grains (~50 nm) in the vicinity of shear bands and recovered parent grains (10–35 μm) with pre-existing nano-twins. Upon annealing, trimodal microstructures were created via partial recrystallization, characterized by small recrystallized grains (<1 μm) associated with shear bands, medium-sized grains (1–6 μm) recrystallized through subgrain rotation or coalescence of parent grains and retained large un-recrystallized grains.

The enormous improvement in yield strength of the bimodal microstructure from 555 MPa to 1.3 GPa relative to the 95 vol % recrystallized specimen (with an average grain size of 2.2 μm) was attributed to the appearance of pre-existing nano-twins and nanosized grains.

In specimens with trimodal microstructures, ductility was improved from 14% to 60% compared to those with bimodal microstructures due to the appearance of a multistage work hardening behavior. Specimens with less than 55% recrystallization exhibited three stages of strain hardening, whereas for those containing 85% recrystallization and above, four-stage work hardening behavior was observed with a steep increase at low strains (2–5%). This work hardening sequence was due to the activation of TRIP and TWIP effects over a large strain regime, which was associated with the difference in phase stability promoted by the grain size

hierarchy. Particularly, the resistance to the decrease of the work hardening rate in the last stage of strain hardening was attributed to the formation of martensite and twins in grains of sub-micrometer size (<500 nm).

Acknowledgements

The financial support of the German Research Foundation (Deutsche Forschungsgemeinschaft, DFG) within the Priority Programme 2006 (Compositionally Complex Alloys – High Entropy Alloys) is acknowledged. The authors would like to gratefully acknowledge Dr. Xiaoxiang Wu for the help of TEM analysis and the kind support of M. Nellessen, K. Angenendt, M. Adamek, and B. Breitbach at the Max-Planck-Institut für Eisenforschung.

Appendix

A. Calculation of the critical stresses for the formation of HCP-martensite and twins

It has been well established that activation of TRIP and TWIP effects strongly depends on the stacking fault energy (SFE). TRIP is normally found in the FCC structured metals with SFE below 20 mJ/m^2, while TWIP was reported in the materials with higher SFE between 18 and 40 mJ/m^2 [49,50]. The SFE of the present iHEA is expected to be around 18–20 mJ/m^2, since TRIP and TWIP mechanisms occurred concurrently upon deformation and no B.C.C. α'-martensite was observed [51]. The SFE of Fe-30Mn-0.5C (at.%) was found to be around 20 mJ/m^2 [49,52] and Co and Cr are both HCP-phase stabilizing elements and thus decrease the SFE [51,53]. Therefore, the SFE of the 49.5Fe-30Mn-10Co-10Cr-0.5C (at.%) iHEA is assumed to be 18 mJ/m^2 for the following calculation. The SFE, Γ_{sf}, can be determined by equation (6), as below:

$$\Gamma_{sf} = 2\rho_m \Delta G^{FCC\rightarrow HCP} + 2\sigma^{FCC/HCP} \tag{6}$$

Here, $\Delta G^{FCC\rightarrow HCP}$ is the Gibbs free energy difference between the FCC phase and the HCP-martensite, $\sigma^{FCC/HCP}$ is the interface energy (5–15 mJ/m^2), and ρ_m is the molar surface density of the {111} plane (2.94×10^{-5} mol/m^2). Therefore, $\Delta G^{FCC\rightarrow HCP}$ can be derived from equation (6) with taking the interface energy of 10 mJ/m^2.

According to the HCP-martensite nucleus model proposed by Mahajan et al. [18], the formation of HCP-phase involves Shockley partial dislocations gliding on every second (111) plane. The critical stress for the growth of the HCP-nucleus can be expressed by equation (7):

$$\tau_{tr} = \frac{2\sigma^{\gamma/\varepsilon}}{3b_{tr}} + \frac{3Gb_{tr}}{L_{tr}} + \frac{h\Delta G^{F.C.C.\rightarrow H.C.P.}}{3b_{tr}} \tag{7}$$

Here, G is the shear modulus, b_{tr} is the Burgers vector of the partial dislocation (0.147 nm) and L_{tr} is the length of the nucleus.

Formation of deformation twins in FCC also involves $\frac{a}{6}<11\bar{2}>$ Shockley partials but gliding on the successive {111} plane, suggested by Mahajan and Chin [19]. The critical stress for twin growth, τ_{tw}, can be estimated by equation (8) [25]:

$$\tau_{tw} = \frac{\Gamma_{sf}}{3b_s} + \frac{3Gb_s}{L_0} \tag{8}$$

Here, L_0 is the width of twin embryo (260 nm) [25]. At the SFE of 18 mJ/m^2, the shear stress required to grow martensite and twins are very close, about 174 MPa. By considering a Taylor factor of 3.06, a normal stress of 531 MPa is required to grow HCP-martensite and twins. The lowest yield strength among all the annealed specimens was 555 MPa in this work, thus the predicted stresses for HCP-martensitic transformation and twinning both below the bulk yield stresses.

References

[1] B. Cantor, et al., Microstructural development in equiatomic multicomponent alloys, Mater. Sci. Eng. A 375–377 (2004) 213–218.
[2] B. Gludovatz, et al., A fracture-resistant high-entropy alloy for cryogenic applications, Science 345 (6201) (2014) 1153–1158.
[3] D.B. Miracle, O.N. Senkov, A critical review of high entropy alloys and related concepts, Acta Mater. 122 (2017) 448–511.
[4] W. Zhang, P.K. Liaw, Y. Zhang, Science and technology in high-entropy alloys, Sci. China Mater. 61 (1) (2018) 2–22.
[5] J.-W. Yeh, et al., Nanostructured high-entropy alloys with multiple principal elements: novel alloy design concepts and outcomes, Adv. Eng. Mater. 6 (5) (2004) 299–303.
[6] J.Y. He, et al., A precipitation-hardened high-entropy alloy with outstanding tensile properties, Acta Mater. 102 (2016) 187–196.
[7] Z. Li, et al., Interstitial atoms enable joint twinning and transformation induced plasticity in strong and ductile high-entropy alloys, Sci. Rep. 7 (40704) (2017) 1–7.
[8] Z. Li, et al., Metastable high-entropy dual-phase alloys overcome the strength–ductility trade-off, Nature 534 (2016) 227.
[9] Z. Li, et al., Ab initio assisted design of quinary dual-phase high-entropy alloys with transformation-induced plasticity, Acta Mater. 136 (2017) 262–270.
[10] Y. Deng, et al., Design of a twinning-induced plasticity high entropy alloy, Acta Mater. 94 (2015), p. 124-`33.
[11] N.D. Stepanov, et al., Effect of thermomechanical processing on microstructure and mechanical properties of the carbon-containing CoCrFeNiMn high entropy alloy, J. Alloy. Comp. 693 (2017) 394–405.
[12] D. Li, et al., High-entropy Al0.3CoCrFeNi alloy fibers with high tensile strength and ductility at ambient and cryogenic temperatures, Acta Mater. 123 (2017) 285–294.
[13] T. Bhattacharjee, et al., Simultaneous strength-ductility enhancement of a nano-lamellar alcocrfeni2.1 eutectic high entropy alloy by cryo-rolling and annealing, Sci. Rep. 8 (2018) 3276.
[14] K. Lu, Stabilizing nanostructures in metals using grain and twin boundary architectures, Nat. Rev. Mater. 1 (2016) 1–13.
[15] M. Wang, Z. Li, D. Raabe, In-situ SEM observation of phase transformation and twinning mechanisms in an interstitial high-entropy alloy, Acta Mater. 147 (2018) 236–246.
[16] C.-S. Yoo, et al., Effect of grain size on transformation-induced plasticity in an ultrafine-grained metastable austenitic steel, Scr. Mater. 59 (2008) 71–74.
[17] K.M. Rahman, V.A. Vorontsov, D. Dye, The effect of grain size on the twin initiation stress in a TWIP steel, Acta Mater. 89 (2015) 247–257.
[18] S. Mahajan, M.L. Green, D. Brasen, A model for the FCC HCP transformation, its applications, and experimental evidence, Metall. Tran. A 8A (1977) 283–293.
[19] S. Mahajan, G.Y. Chin, formation of deformation twins in F.C.C. Crystals, Acta Metall. 21 (1973) 1353–1363.
[20] S.L. Wong, et al., A crystal plasticity model for twinning- and transformation-induced plasticity, Acta Mater. 118 (2016) 140–151.
[21] I. Gutierrez-Urrutia, S. Zaefferer, D. Raabe, The effect of grain size and grain orientation on deformation twinning in a Fe–22 wt.% Mn–0.6 wt.% C TWIP steel, Mater. Sci. Eng. A 527 (2010) 3552–3560.
[22] Y.-S. Jung, Y.-K. Lee, Effect of pre-deformation on the tensile properties of a metastable austenitic steel, Scr. Mater. 59 (2008) 47–50.
[23] K. Sipos, L. Remy, A. Pineau, Influence of austenite predeformation on mechanical properties and strain-induced martensitic transformations of a high manganese steel, Metall. Tran. A 7A (1976) 860–864.
[24] B.C.D. Cooman, Y. Estrin, S.K. Kim, Twinning-induced plasticity (TWIP) steels, Acta Mater. 142 (2018) 283–362.
[25] D.R. Steinmetz, et al., Revealing the strain-hardening behavior of twinning-induced plasticity steels: theory, simulations, experiments, Acta Mater. 61 (2013) 494–510.
[26] I. Gutierrez-Urrutia, D. Raabe, Dislocation and twin substructure evolution during strain hardening of an Fe–22 wt.% Mn–0.6 wt.% C TWIP steel observed by electron channeling contrast imaging, Acta Mater. 59 (2011) 6449–6462.
[27] E. Ma, T. Zhu, Towards strength –ductility synergy through the design of heterogeneous nanostructures in metals, Mater. Today 20 (2017) 323–331.
[28] X. Wu, Y. Zhu, Heterogeneous materials: a new class of materials with unprecedented mechanical properties, Mater. Res. Lett. 5 (8) (2017) 527–532.
[29] M. Koyama, et al., Bone-like crack resistance in hierarchical metastable nanolaminate steels, Science 355 (2017) 1055–1057.
[30] M.-M. Wang, et al., Smaller is less stable: size effects on twinning vs. transformation of reverted austenite in TRIP-maraging steels, Acta Mater. 79 (2014) 268–281.
[31] M.-M. Wang, et al., Nanolaminate transformation-induced plasticity–twinning-induced plasticity steel with dynamic strain partitioning and enhanced damage resistance, Acta Mater. 85 (2015) 216–228.
[32] M. Calcagnotto, et al., Orientation gradients and geometrically necessary dislocations in ultrafine grained dual-phase steels studied by 2D and 3D EBSD, Mater. Sci. Eng. A 527 (2010) 2738–2746.
[33] G.B. Olson, M. Cohen, A mechanism for the strain-induced nucleation of

martensitic transformations, J. Less Common. Met. 28 (1972) 107–118.
[34] N. Hansen, D.A. Hughes, Analysis of large dislocation populations in deformed metals, Phys. Stat. Sol. (b) 149 (1995) 155–172.
[35] J.F.C. Lins, et al., A microstructural investigation of adiabatic shear bands in an interstitial free steel, Mater. Sci. Eng. A 457 (2007) 205–218.
[36] N. Jia, et al., Non-crystallographic shear banding in crystal plasticity FEM simulations: example of texture evolution in a-brass, Acta Mater. 60 (2012) 1099–1115.
[37] H.T. Wang, N.R. Tao, K. Lu, Strengthening an austenitic Fe–Mn steel using nanotwinned austenitic grains, Acta Mater. 60 (2012) 4027–4040.
[38] K. Tao, H. Choo, H. Li, Transformation-induced plasticity in an ultrafine-grained steel: an in situ neutron diffraction study, Appl. Ph. Lett. 90 (2007) 101911.
[39] Z. Wang, et al., The effect of carbon on the microstructures, mechanical properties, and deformation mechanisms of thermo-mechanically treated Fe40.4Ni11.3Mn34.8Al7.5Cr6 high entropy alloys, Acta Mater. 126 (2017) 346–360.
[40] F. Otto, et al., The influences of temperature and microstructure on the tensile properties of a CoCrFeMnNi high-entropy alloy, Acta Mater. 61 (2013) 5743–5755.
[41] H. Gao, Y. Huang, Geometrically necessary dislocation and size-dependent plasticity, Scr. Mater. 48 (2003) 113–118.
[42] D. Jorge-Badiola, A. Iza-Mendia, I. Gutierrez, Study by EBSD of the development of the substructure in a hot deformed 304 stainless steel, Mater. Sci. Eng. A 394 (2005) 445–454.
[43] T.H. Courtney, Mechanical Behavior of Materials, second ed., Waveland Press, Inc, Long Grove, IL, USA, 2005.
[44] E. Demir, et al., Investigation of the indentation size effect through the measurement of the geometrically necessary dislocations beneath small indents of different depths using EBSD tomography, Acta Mater. 57 (2009) 559–569.
[45] J. Kadkhodapour, et al., Experimental and numerical study on geometrically necessary dislocations and non-homogeneous mechanical properties of the ferrite phase in dual phase steels, Acta Mater. 59 (2011) 4387–4394.
[46] G.E. Dieter, Mechanical Metallurgy, third ed., McGraw-Hili Book Co, New York, 1986.
[47] D. Raabe, et al., Designing ultrahigh strength steels with good ductility by combining transformation induced plasticity and martensite aging, Adv. Eng. Mater. 11 (7) (2009) 547–555.
[48] C. Herrera, D. Ponge, D. Raabe, Design of a novel Mn-based 1 GPa duplex stainless TRIP steel with 60% ductility by a reduction of austenite stability, Acta Mater. 59 (2011) 4653–4664.
[49] S. Allain, et al., Correlations between the calculated stacking fault energy and the plasticity mechanisms in Fe–Mn–C alloys, Mater. Sci. Eng. A 387–389 (2004) 158–162.
[50] Z. Li, D. Raabe, Strong and ductile non-equiatomic high-entropy alloys: design, processing, microstructure, and mechanical properties, JOM 69 (11) (2017) 2099–2106.
[51] A. Dumay, et al., Influence of addition elements on the stacking-fault energy and mechanical properties of an austenitic Fe–Mn–C steel, Mater. Sci. Eng. A 483–484 (2008) 184–187.
[52] A. Saeed-Akbari, et al., Derivation and variation in composition-dependent stacking fault energy maps based on subregular solution model in high-manganese steels, Metall. Mater. Tran. A 40A (2009) 3076–3090.
[53] S. Lu, et al., Stacking fault energies of Mn, Co and Nb alloyed austenitic stainless steels, Acta Mater. 59 (2011) 5728–5734.